Architecturally Simple Organic Photodiodes with Highly Competitive Figures of Merit via Facile Self-Assembly Strategy

Hrisheekesh Thachoth Chandran [a,#], Hua Tang [a,b,#], Taili Liu [c,d], Sudhi Mahadevan [e], Kuan Liu [a], Zhen Lu [a], Jiaming Huang [a], Zhiwei Ren [a], Fuyou Liao [f], Yang Chai [f], Patrick WK Fong [a], Sai-Wing Tsang [e], Shirong Lu [b], Gang Li [a,*]

[a]*Department of Electronic and Information Engineering, Research Institute for Smart Energy (RISE), The Hong Kong Polytechnic University, Hung Hom, Kowloon, Hong Kong SAR, P. R. China.*

[b]*Thin-film Solar Technology Research Center, Chongqing Institute of Green and Intelligent Technology, Chinese Academy of Sciences, Chongqing, 400714, P. R. China.*

[c]*College of Physics and Electronic Information, Yunnan Normal University, Yunnan Kunming 650500, China.*

[d]*Yunnan Provincial Key Laboratory for Photoelectric Information Technology, Yunnan Normal University, Yunnan Kunming 650500, China*

[e]*Department of Materials Science and Engineering, Center of Super-Diamond and Advanced Films (COSDAF), City University of Hong Kong, Hong Kong SAR, P. R. China.*

[f]*Department of Applied Physics, The Hong Kong Polytechnic University, Hung Hom, Kowloon, Hong Kong SAR, P. R. China.*

#These authors contributed equally to this work

Corresponding author Email: gang.w.li@polyu.edu.hk

Abstract

Photodetectors (PDs) based on organic materials exhibit potential advantages such as low-temperature processing, superior mechanical properties, and form factors. They have seen rapid strides toward achieving performance metrics comparable to inorganic counterparts. Here, a simplified device architecture is employed to realize stable and high-performance organic PDs (OPDs) while further easing the device fabrication process. In contrast to the sequential deposition of the hole blocking layer (HBL) and active layer (conventional 'two-step' processing), the proposed strategy forms self-assembled HBL and active layer in a 'single-step' processing. A high-performance UV-Vis-NIR OPD based on PM6:BTP-eC9 system is demonstrated using this cost-effective processing strategy. The green solvent processed proof-of-concept device exhibits remarkable responsivity of ~0.5 A W^{-1}, lower noise current than conventional two-step OPD, ultrafast rise/fall times of 1.4/1.6 µs (comparable to commercial silicon diode), and a broad linear dynamic range of 140 dB. Importantly, highly stable (light and heat) devices compared to those processed by the conventional method are realized. The broad application potential of this elegant strategy is proven by demonstrating the concept in three representative systems with broadband sensing competence.

Introduction

Organic material-based photodetectors (PDs) are emerging as an exciting candidate for applications in health monitoring, biomedical imaging, near-infrared sensing, and so on.[1-3] Although silicon-based photodetectors are still the preferred photodetection technology for UV-Vis-NIR light, organic photodetectors (OPDs) have advantages like low-temperature processing, appealing mechanical properties, and form factors (size and shape) for a variety of emerging applications.[4-10] To match with silicon PD, prior efforts in OPD research were mainly focused on performance metrics improvements.[2, 11-13] Recently, Fuentes-Hernandez and co-workers found

that the performance metrics (except rise time) of an optimized OPD can rival that of low-noise silicon diodes within the visible spectral range.[9] This rapid and impressive progress demands advancements in other aspects that define the market potential of OPD.[14] These include a fair balance between sensitivity and response speed, ease of fabrication, low cost, green solvent processability, light/heat stability, etc.[15-17] However, these factors were relatively underexplored in comparison to the performance improvement.[2] While retaining the high-performance metrics and stability, realizing architectural simplicity is imperative to keep up with the already matured fabrication process of silicon PDs.[2]

Considering the NIR sensing into account, OPD performance is yet to match with the inorganic counterparts. Due to its substantial success in state-of-the-art organic photovoltaic (OPV) devices, non-fullerene acceptors (NFA) should be the ideal choice for NIR OPDs and have drawn significant attention in recent years.[18, 19] Wide range of versatile NFAs offer potential advantages including high light absorption coefficient, tunable absorption range and energy level, favorable molecular packing, lower disorder, etc.[20-22] However, in comparison to fullerene acceptor-based OPDs, the NFA-based systems face a critical challenge in terms of the limited availability of suitable hole-blocking-layer (HBL) materials. Most of the high performance inverted OPDs reported so far are based on polyethylenimine ethoxylated (PEIE) or PEIE modified zinc oxide (ZnO) as HBL/interface layer[9, 12, 23], but were found not suitable for PDs using state-of-the-art 1,1-dicyanomethylene-3-indanone end groups materials in the active layer, which was shown to chemically react with PEIE.[9, 24] Thus, expanding the library of HBL materials suitable for NFA based OPD systems is also crucial for the advancements in NIR sensing.

Herein, we present a simple self-assembly strategy to simultaneously achieve architectural simplicity, competitive performance metrics (both sensitivity and speed), robust stability and green

solvent processability in NIR sensitive organic photodiodes. In the proposed architecture, instead of depositing the HBL as a separate layer, the corresponding HBL material is doped into the active layer solution and is deposited in a single step ('self-assembly (SA)' device). This processing strategy can form a self-assembled HBL layer over the glass/ITO substrate and potentially shorten the processing time window/constituent materials to reduce the overall cost of production. Phen-NaDPO (DPO) is used as the HBL material to demonstrate the concept in the PM6:BTP-eC9 material system. DPO is demonstrated as a promising addition to the existing library of HBL materials since it is easily dissolved in hydrocarbon solvents and enables green solvent processability. Interestingly, the self-assembly strategy does not compromise the performance metrics of photodiodes in comparison with the two-step processed 'control' device. Using the simplified device architecture, a UV-Vis-NIR PD is realized with highly competitive performance metrics: responsivity of ~0.5 A W^{-1}, low electronic noise current ~2×10^{-13} A $Hz^{-1/2}$, broad linear dynamic range over 140 dB, fast rise/fall times (1.4/1.6 µs), and a -3dB frequency approaching 300 kHz. Moreover, responsivity and rise time are closely comparable to the datasheet specifications of commercial silicon photodiode (Hamamatsu S1133-01). It is important to note that a trade-off typically exists between specific detectivity and the speed of the detector. However, the present work has simultaneously maintained competitive speed and detectivity while employing a much simple device architecture. Along with competitive performance metrics, robust heat stability is also observed in the 'self-assembled' device compared to the 'control' device. The high performance of the SA device can be attributed to suppressed shunt pathways and lower trap density. In addition, preliminary studies in two exemplary OPDs, fullerene (P3HT:$PC_{71}BM$) and non-fullerene (PM6:IT-2F) acceptor-based systems, hint that the simplified device architecture can be effective in a diverse array of material systems. This novel device processing strategy

synchronously results in stable, competitive-performance, and cost-effective organic PDs and renders them one step closer to silicon PDs.

Experimental section

Materials: PM6, BTP-eC9 and IT-2F were obtained from Solarmer Material Inc. $PC_{71}BM$ was purchased from LumTec. Highly regioregular P3HT was obtained from Rieke Metals. Phen-NaDPO was purchased from 1 Material Tech Inc. The solvents (o-xylene, chlorobenzene, 1,2-dichlorobenzene, and isopropanol) and solvent additive (1,8-diiodooctane) were purchased from Sigma-Aldrich.

Device fabrication and characterization: Patterned ITO-coated glass substrates (15 Ω sq^{-1}) were cleaned by ultrasonic baths in deionized water, acetone, and isopropanol for 20 minutes each. The cleaned substrates were dried using pressurized nitrogen and subsequently treated using UV-Ozone.[25] Substrates were then transferred to the glove box for HBL and active layer depositions. For control devices, a thin layer of DPO (dissolved in isopropanol with 0.5 mg/ml concentration) is coated over the substrate at 2500 RPM for 30 seconds. For PM6:BTP-eC9 active layer, PM6:BTP-eC9 at 1:1.2 (w/w) donor (D):acceptor (A) ratio is dissolved in o-xylene with a total concentration of 24 mg ml^{-1}. The solution was stirred overnight at 70 ℃ and 0.5% of DIO is added to the active layer solution 30 minutes prior to the deposition. The active layer solution was dynamically spin-coated at 800 RPM for 60 seconds and annealed at 100 ℃ for 10 minutes. For the 'SA' devices, no separate HBL layer deposition is needed. The HBL solution is prepared with a concentration of 0.5 mg ml^{-1} in the same type of solvent that is used for the active layer preparation in 'control' devices (for example, DPO should be dissolved in o-xylene in the case of PM6:BTP-eC9 system) and the DPO solution should be diluted to 0.1 mg ml^{-1} for preparing the active layer solution. The active layer solution for the 'SA' device is prepared by dissolving PM6

and BTP-eC9 in the as-prepared DPO containing o-xylene with a 1:1.2 D:A ratio (total concentration: 24 mg ml^{-1}). Deposition and annealing conditions of the 'SA' device active layer are identical to the 'control' device. Following the active layer deposition, substrates were loaded into the thermal evaporation chamber for the deposition of a thin layer of MoO_3 and a 90 nm thick Ag electrode. The active area of the as-prepared device is 0.05 cm^2. The thickness of both control and SA devices is ~240 nm.

Active layers processing for other representative systems used in this study are as follows. For P3HT:PC_{71}BM active layer, P3HT:PC_{71}BM were mixed at 1:1 (w:w) ratio to a total concentration of 75 mg ml^{-1} in 1,2-dichlorobenzene, stirred overnight at 70°C and filtered using a PTFE filter (0.2 μm) prior to use. The deposition was done at 800 RPM with an acceleration of 2000 RPM and annealed at 150 ℃ for 10 minutes. For PM6:IT-2F active layer, materials were mixed at 1:1 D:A ratio (total concentration of 30 mg ml^{-1}) in chlorobenzene and stirred overnight at 40 ℃. Dynamic spin coating at 1200 RPM for 60 seconds is employed and the film was annealed at 100 ℃ for 10 minutes. For SA devices, active layer solutions were prepared in solvents containing DPO at a concentration of 0.1 mg ml^{-1}.

The current density-voltage (*J*-*V*) measurements under dark/illumination were carried out using a Keithley 2400 source meter. The AM 1.5G solar spectrum was simulated using an Enlitech solar simulator. Biased EQE and responsivity were measured using an Enlitech spectral response measurement system QE-R (Enlitech Co., Ltd.) at 180 Hz chopper frequency. Noise current was measured under dark conditions using a lock-in amplifier (Stanford research systems SR830) and the corresponding value at 180 Hz is used for further calculations to match with the equivalent noise bandwidth of responsivity measurements.[26] A custom-written LabVIEW program is used for

data acquisition. The contact angles of the films were measured using DSA-100 (KRUSS Germany) contact angle meter.

The frequency response of the PD was measured by illuminating the device with a square wave modulated 830 LED light at different frequencies. A low-noise pre-amplifier was used to amplify the signal from the OPD and the amplified transient was then recorded by the oscilloscope (Tektronics MDO 3024). The OPD was biased at -0.1V using the low-noise preamplifier.

Linear dynamic range measurement was carried out by illuminating the PD device using 830 nm monochromatic light with variable irradiance. The irradiance was varied by placing a set of neutral-density filters (Thorlabs). A calibrated silicon detector (Thorlabs) was used for the input power measurement and the photo response (at -0.1V) was measured using a lock-in amplifier (Standard Research SR830). A custom-written LabVIEW program is used for data acquisition.

Highly sensitive EQE measurements were conducted with a home-built setup and are described in previous works.[27, 28] The setup is equipped with a light source (1000W Xenon Arc Lamp, Newport), monochromator (Zolix), optical chopper (ThorLabs), lock-in amplifier (Standard Research SR830), low noise current pre-amplifier (Standard Research SR570), and calibrated silicon and germanium detectors (ThorLabs).[27]

Results and discussions

Two types of devices fabricated in this study are designated as follows: Type-1: Indium tin oxide (ITO)/HBL/Active layer/ molybdenum oxide (MoO_3)/Ag (hereon referred to as control device) and Type-2: ITO/HBL doped Active layer/MoO_3/Ag (hereon referred to as self-assembled (SA) device). The active layer comprises a polymer donor (PM6) and a non-fullerene acceptor (BTP-eC9), both are state-of-the-art materials in organic photovoltaic (OPV) cells.[29] Phen-NaDPO (DPO) is used as the HBL and MoO_3 is serving as the hole transport layer/electron blocking layer.

It is to be noted that the HBL used in this study, DPO, is employed in high-performance OPV devices as an electron transport layer, but rarely used in OPDs.[30-32] DPO is easily dissolved in hydrocarbon solvents and makes it a potential alternative to the existing HBL materials for OPD. The device architecture of the 'SA' device and chemical structures of active layer materials and HBL are given in Fig. 1a. The flat band energy level alignments of the corresponding materials are depicted in Fig. 1b.[33-35] The two types of devices are differed by the way HBL is deposited. For the 'control' device, DPO is deposited over the glass/ITO substrate as a stand-alone HBL and is followed by the deposition of an active layer solution. For the 'SA' device, DPO is doped into the active layer solution and is deposited as a simple single-step deposition (HBL+active layer) over glass/ITO substrate. For the SA device, the HBL and active layer are processed from the non-toxic hydrocarbon solvent (o-Xylene). Subsequently, thermal evaporation is used to deposit MoO_3 and Ag. The self-assembly method may considerably reduce the cost of processing by reducing the preparation time window and constituent materials. From the absorption spectra given in Fig. S1, a strong NIR absorption extending over 900 nm is observed for both BHJ blends (PM6:BTP-eC9 (control) and DPO-doped PM6:BTP-eC9 (SA) blends).

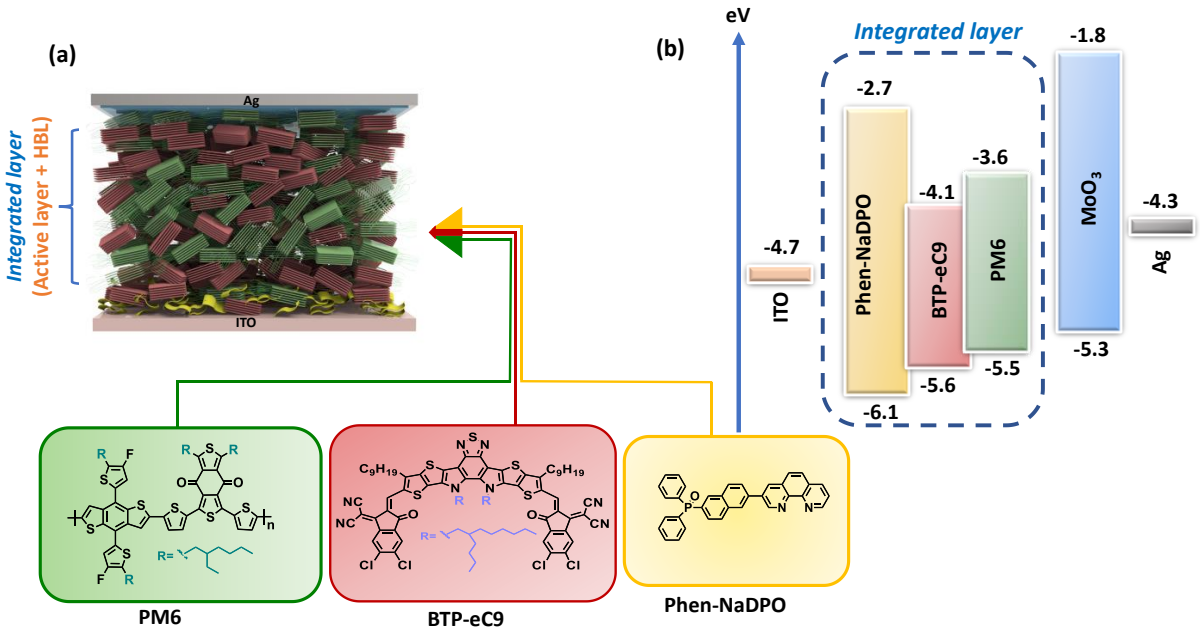

Fig. 1 (a) Chemical structures of the donor (PM6), acceptor (BTP-eC9), and HBL (Phen-NaDPO) materials and the simplified scheme of 'SA' device architecture. Layer thickness is not drawn to scale. (b) Flat band energy level diagram of the materials used in the PM6:BTP-eC9 PD device.

To understand the vertical distribution of DPO in the 'SA' device, the time-of-flight secondary ion mass spectrometry (TOF-SIMS) is performed. Two elements were mainly tracked: PO_3^- and InO^-. The emergence of InO^- indicates that the ITO substrate is approaching and the presence of PO_3^- shows the distribution of DPO in the film. From Fig. 2a, it is seen that PO_3^- is detected near the surface of ITO and the peak is getting strengthened near the region where InO^{-1} is peaking. These observations indicate that the DPO is self-assembled near the ITO surface as a DPO-rich domain. To further understand the driving force for the self-organization of DPO near the surface of ITO, the surface free energy of the neat ITO, DPO and active layer (PM6:BTP-eC9) substrates are calculated. Surface free energy is an important parameter to characterize the solid surface and its interaction with other materials.[36] Solid surface free energy can be derived using

the contact angles and surface tension components of the standard probe liquids via the Owens–Wendt approach using the following equation

$$\gamma_{\mathrm{L}}.(\cos\theta + 1) = 2\,.\left(\gamma_{\mathrm{L}}^{\mathrm{d}}\,.\,\gamma_{\mathrm{S}}^{\mathrm{d}}\right)^{1/2} + 2\,.\left(\gamma_{\mathrm{L}}^{\mathrm{p}}\,.\,\gamma_{\mathrm{S}}^{\mathrm{p}}\right)^{1/2} \quad (1)$$

Where γ_L is the surface tension of the liquid, γ_S is the surface energy of the solid, θ is the contact angle formed by the liquid on the solid.[37-40] The surface free energy of a solid or liquid is considered as the sum of contributions arising from the dispersive component (γ^d) and polar component (γ^p) of the free energy ($\gamma = \gamma^d + \gamma^p$). The dispersive and polar components of free energy of the many well-chosen standard probe liquids (here water and ethylene glycol (EG)) are available in the literature. The surface tension components (in units of mN m^{-1}) of the standard liquids are adopted from the literature (γ^d of 21.8 mN m^{-1} and γ^p of 51.0 mN m^{-1} for water and of γ^d of 29.0 mN m^{-1} and γ^p of 19.0 mN m^{-1} for EG).[38] Fig. 2b and Table S1 show the contact angles right after the standard liquids are dropped over the substrate. In order to improve the accuracy of the calculation, the average of 3 contact angles is used for the calculation of surface free energy. The surface free energy estimated using the above-mentioned method is respectively 58.7 mJ m^{-2}, 46.3 mJ m^{-2} and 19.1 mJ m^{-2} for ITO, DPO and active layer substrates. The surface free energy of ITO and DPO are typically on the higher side and the surface energy of DPO is ~2.5 times higher than the surface energy of the active layer substrate. The high surface energy of DPO can drive the migration of DPO towards the bottom of the film (near the surface of ITO) in the 'SA' device to form self-assembled HBL and these results are in good agreement with TOF-SIMS data. To further strengthen this hypothesis, contact angle at different time intervals is measured to study the time dependence of contact angle.[40] The initial contact angle, which is determined immediately after the standard liquid is dropped, is followed by further measurements every

minute for a total of two minutes. The change in contact angle is typically limited to ±6% from the initial value, ensuring the validity of the proposed self-assembly mechanism.

Next, current density (dark/illumination), external quantum efficiency (*EQE*) and spectral responsivity (*R*) of the 'control' and 'SA' devices are compared. Fig. 2c shows the typical dark and light current density-voltage (*J*-*V*) curves of 'control' and 'SA' devices. The 'SA' device has, in comparison, quite a lower mean dark current density (J_d) than that in 'control' OPD: from the statistical analysis (Fig. S3a), the mean J_d value for the 'control' device is ~100 nA cm^{-2} and is about 30 nA cm^{-2} for the SA device. Nevertheless, both devices have comparable photocurrent density (J_{ph}) in the reverse bias region. *EQE* (measured at -0.1V bias and 180 Hz chopping frequency) of both types of devices are almost identical and the values are consistently above 70% across a wide wavelength range (350-890 nm) (Fig. S3b). Maximum *EQE* stood above 80% in both types of devices. Next, the *R* can be found from the *EQE* spectra using the following equation

$$R = EQE \times {}^{q\lambda}/_{hc} \tag{2}$$

where q is the electronic charge, λ is the wavelength, h is the plank's constant and c is the velocity of light. From the *R* spectra shown in Fig. 2d and the statistical analysis shown in Fig. S3c, 'control' and 'SA' devices exhibit peak value ~0.5 A W^{-1}, which is typically among the highest values reported so far.[13, 41] It is worth noting that the *R* value of 0.5 A W^{-1} is better than the commercially available Hamamatsu S1133-14 silicon photodiode and is in close comparison with Hamamatsu S1133-01. Considering the fundamental challenges associated with narrow bandgap materials to simultaneously realize low noise current/dark current and high NIR photoresponse, the performance metrics of these devices are quite impressive.[1, 12, 42] Both types of devices exhibit highly similar fundamental performance metrics, with J_d as an exception where the 'SA' device performs better. This reduced J_d in the 'SA' device may positively impact the key detection

parameter "specific detectivity", as discussed in the later section.[41, 43] To further confirm the function of DPO as HBL in 'control' and 'SA' devices, a device without the DPO layer ('No HBL' device) is also fabricated with the following structure for a fair comparison: ITO/PM6:BTP-eC9/MoO_3/Ag. The J_d of 'No HBL' device is more than two orders larger than the 'control' and 'SA' devices (Fig. S4a). The *EQE* and *R* of 'No HBL' device are also inferior to the other types of devices fabricated in this study (Fig. S4(b-c)). These results solidify the important role of DPO as HBL in the proposed device architecture.

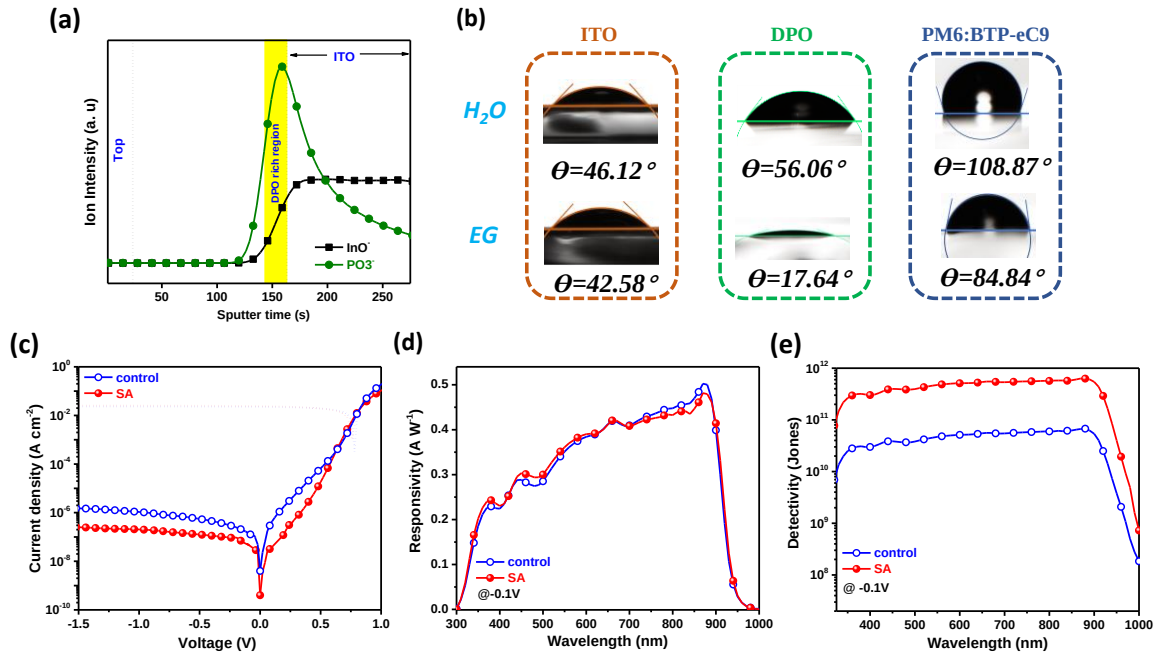

Fig. 2 (a) TOF-SIMS ion yield of PO_3^- and InO^- as a function of sputtering time for blend films with self-assembly architecture. (b) The H_2O and EG contact angles of ITO, DPO and PM6:BTP-eC9 blend films. (c) *J-V* curve of the 'control' and 'SA' devices under dark (solid line with symbols) and 1-sun illumination (dotted line). (d) Responsivity and (e) experimentally measured specific detectivity of the 'control' and 'SA' devices at -0.1V bias.

Specific detectivity (D^*) is considered to be the key metric of photodetection and it denotes the ability of the PD to detect faint optical signals.[41] D^* is directly related to the R and noise characteristics of the photodiode. It is crucial to note that there are various detectivity estimation methods available, and the resulting values vary greatly depending on the approach used for estimation.[44] This has caused various exaggerated and may be erroneous claims of record-high performance metrics to appear in the literature and a reasonable comparison between the values is increasingly getting difficult.[44] For a careful derivation of detectivity, a lock-in amplifier set-up is used to accurately probe the electronic noise characteristics and the D^* is found using equation (3).[2]

$$D^* = \frac{\sqrt{A}}{NEP} \tag{3}$$

where A is the device area in cm^2 and *NEP* is the Noise Equivalent Power in units of W $Hz^{-1/2}$.[2] *NEP* denotes the minimum amount of light that can be detected at a signal-to-noise ratio of 1 for a 1 Hz integration bandwidth.[2]

$$NEP = \frac{i_n}{R} \tag{4}$$

where R is the responsivity in A W^{-1} and i_n is the noise current in A $Hz^{-1/2}$. For the 'SA' device biased at -0.1V, the lowest i_n at 180 Hz is around 2.0×10^{-13} A $Hz^{-1/2}$ and the mean value is ~3.0×10^{-13} A $Hz^{-1/2}$ (Fig. S5a and Fig. S5c). The *NEP* value stands at 4.1×10^{-13} W $Hz^{-1/2}$. For calculating the *NEP*, the R at optical power >1nW is considered. D^* derived from these experimentally measured noise characteristics is shown in Fig. 2e. It is interesting to observe that the D^* value holds a maximum value of 7.1×10^{11} Jones at ~880 nm and is consistently over 3×10^{11} Jones (1 Jones= 1 $cmHz^{1/2}W^{-1}$) throughout the wavelength range (350 nm to 925 nm), demonstrating its

application potential in broadband weak light sensing. The mean D^* value stood at 4.5×10^{11} Jones (Fig. S5d). For the 'control' device, the i_n is larger than the 'SA' device (Fig. S5b) and consequently reduces the maximum D^* to 7.0×10^{10} Jones (Fig. 2e and Fig. S5d). Alternatively, D^* can also be estimated from the shot noise and/or thermal noise characteristics, a simple approach typically used in many reported works.[2] If D^* is calculated from white noise (shot noise+thermal noise),[2] the value comes around ~10^{13} Jones for 'SA' devices (at -0.1V bias). However, the reliable scientific practice is to estimate the D^* from experimentally measured noise characteristics as the D^* estimated from white noise may be prone to overestimation.[44]

The linear dynamic range (*LDR*) represented in dB describes the range within which the detector output scales linearly with the input irradiance.[12] *LDR* is calculated using equation (5).[12, 26, 45]

$$LDR = 20log\frac{J_{upper}}{J_{lower}} = 20log\frac{L_{upper}}{L_{lower}} \quad (5)$$

where J stands for photocurrent density in A cm^{-2} and L denotes light intensity in W cm^{-2}. LDR is determined by illuminating the OPD with an above bandgap 830 nm monochromatic light across an intensity range from 3×10^{-9} W cm^{-2} to 3×10^{-2} W cm^{-2}. For the 'SA' device, the photocurrent density scales linearly across the varying input irradiance range, resulting in an *LDR* of ≥140 dB (Fig. 3a). In comparison, the LDR of the 'control' device is around 126 dB (Fig. S6a).

Next, the response speed of the photodetector is evaluated. The transition time between 10% of the minimum current to 90% of the maximum current (rise time (t_{rise})), and from 90% down to 10% (fall time (t_{fall})) is obtained by illuminating the device with a time-varying square wave light signal (830 nm LED).[26] As detailed in Fig. 3b, 'SA' PD exhibits an ultrafast t_{rise} of 1.4

µs and t_{fall} of 1.6 µs, outmatching the majority of the OPDs.[2, 46] These values are 1.8 µs and 2.1 µs respectively for 'control' device, marginally slower than the 'SA' devices (Fig. S6b). -3dB frequency (f_{-3dB}), another important performance metric of PD, is defined as the bandwidth at which the amplitude of the signal is attenuated to -3dB from the original maximum amplitude.[12] The photoresponse was recorded at various light modulation frequencies to find the corresponding normalized values. The f_{-3dB} is found to be around ~290 kHz for the 'SA' device (Fig. 3c) and 240 kHz for the control device (Fig. S6c). t_{rise}, t_{fall} and f_{-3dB} values of the 'SA' device denote the characteristics of an ultrafast PD and are largely similar to commercial Hamamatsu S1133-01 silicon photodiode. Overall, the performance metrics of SA devices are comparable to or at best better than the control devices and is typically among the best reported values in the literature (Table-S2).

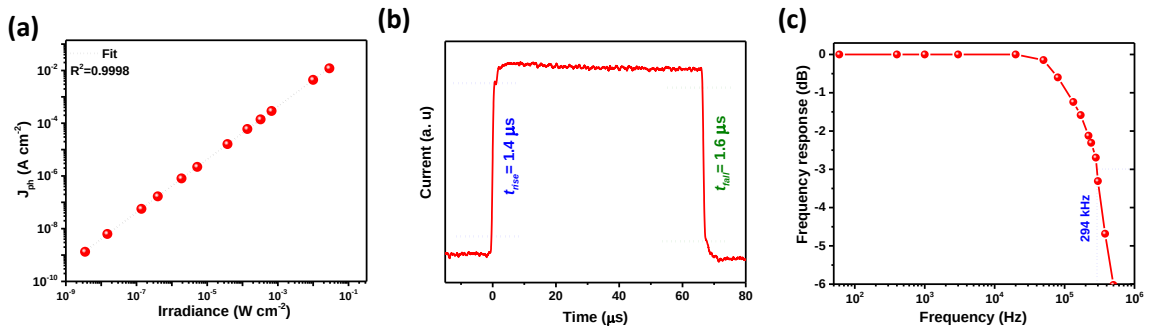

Fig. 3 (a) Photocurrent density linearity upon varying the 830 nm light input irradiance at -0.1V bias, (b) rise time/fall time and (c) -3dB frequency of the 'SA' device.

Although promising advances have been achieved in terms of performance, device stability is a major concern in organic materials-based optoelectronic devices.[47, 48] The degradation in OPDs is attributed to the combined effects of multiple factors, mainly light and heat.[20] Detrimental sensitivity of J_d to illumination history is considered as a hurdle to achieve consistent figures-of-

merit.[49] In this regard, the stability of the PD devices to illumination history is studied in terms of J_d. For a reasonable comparison of stability, along with 'SA' devices, 'control' devices and 'ZnO HBL' based devices are studied. It is to be noted that all these devices are having identical device structure, except the way HBL materials are employed. The photodiode's light stability in terms of J_d is assessed every 30 minutes for a total of 2 hours of light stress, and the values of dark current at -0.1V bias are statistically compared with that of before illumination. It is recently reported that the J_d reliability before and after light illumination is an issue of concern for the ZnO HBL, one of the most widely used HBL in OPD devices.[12, 20, 49, 50] It is evident from Fig. S7a that the 'SA' device has excellent J_d reliability before/after white light illumination (1×10^{-1} W cm^{-2}, 120 minutes). The 'control' device also possesses good J_d reliability (Fig. S7b). After the first 30 minutes of light stress, both the SA and the control device have a slight rise in dark current, but the change gradually reaches saturation after that. On the other hand, in agreement with the literature, J_d of ZnO based PD is severely affected with ~1 order increase in J_d after the illumination (Fig. S7c). Another operational stressor for organic PD is "heat". To endure module packaging, the temperature stability of organic PDs must be taken with vital importance. However, related investigations are concerningly scarce in the literature.[2, 20] We have studied the J_d stability at 100 °C (within the glove box) for a total exposure time of two hours, and the change is measured at every 30 minutes. It is interesting to see from the J_d curves that there is almost no discernible degradation in the 'SA' device (Fig. S8a). In contrast, the dark *J-V* of the 'control' device is relatively more sensitive to heating history (Fig. S8b). In the first 60 minutes, there is a noticeable increase in dark current, and the change gradually reaches saturation. ZnO based PD, however, possesses relatively good heat stability (Fig. S8c). In short, the 'SA' device has both robust light and heat stability, and the other devices possess either light/heat stability but lack the other one.

Since the 'SA' device exhibits overall better performance metrics and stability in comparison to the 'control' device, it is imperative to substantiate the mechanism behind the advancement. First, we discuss why 'SA' PD exhibits relatively lower J_d in comparison with the 'control' device. The shunt resistance (R_{sh}) and trap density, two factors that are known to affect the J_d at reverse bias are investigated in detail.[1, 12] R_{sh}, which is found in the vicinity of 0V in the area normalized differential resistance-voltage plot (Fig. 4a), is found to be around 1 order larger for the 'SA' device in comparison to the 'control' device. High R_{sh} indicates that the formation of self-assembled HBL and the active layer is effectively suppressing the leakage pathways. Higher R_{sh} directly translates to lower J_d in 'SA' devices.[12] We assume that the interface between HBL and the active layer in 'control' devices may create possible shunt pathways in contrast to the "self-assembly of HBL" in the 'SA' device. Better coverage of HBL as a "self-assembled DPO rich domain" over ITO may also effectively block the injection of holes into the active layer and thus reduce the reverse bias J_d.

Understanding of traps remains as a heavily debated and controversial topic in organic optoelectronics.[51] The separated charges moving through the percolating paths of BHJ may interfere with defective/impurity sites called traps and are considered as either mid-gap states or shallow tail states lying below the transport gap.[52-54] The presence of traps has important consequences on the electrical response of OPDs.[54] Using the classical P3HT:PCBM organic photodiode system, Fallahpour and co-workers reported that the trap density is a noticeable contributor in controlling the current at lower light intensities or dark.[55] Furthermore, Jonas et.al reported the interplay between the trap state and CT state as a source of J_d.[1] They found that the J_d contains a major contribution from trap-assisted charge carriers and the dark current gets systematically reduced with decreasing concentration of traps.[1] Thus, the trap-states in 'control'

and ‘SA’ devices were probed using ultra-sensitive EQE (s-EQE), a direct probing method that can detect trap/defect states during the operation of the organic PD. Our s-EQE system is capable to probe the sub-picoampere photocurrent generated in the photoexcited trap states.[56] The lower energy part of the sub-gap EQE spectrum belongs to the trap state contribution towards photocurrent.[53] From the normalized s-EQE spectra in the log scale (Fig. 4b), the ‘control’ device is having a higher “low-energy (< 1 eV) sub-gap signal” compared to the ‘SA’ device, denoting higher trap density. In addition to s-EQE measurement, the energetic distribution of trap density (N_t) in ‘control’ and ‘SA’ devices was estimated using admittance spectroscopy. Details of the experiment and fitting model can be found in the reference.[57, 58] From Fig. S9, the trap density of the ‘SA’ device is found to be lower than the ‘control’ device and thus accords well with the observation of lower J_d in the ‘SA’ device. Since the ‘control’ and ‘SA’ devices are mainly differed by the way HBL is processed, we assume that the self-assembly architecture is contributing to the trap-passivation. These results provide a possible and very plausible explanation for the lower J_d in ‘SA’ devices.

Seeking the faster response speed of the SA device in comparison with the control device, atomic force microscopy is employed to understand the effect of morphology on the charge transport, and in general to the overall performance improvement of ‘SA’ devices. From, Fig. S10 (a-b), the SA blend is having a lower root-mean-square roughness (Rq) value of 1.42 nm in comparison with the control blend (2.54 nm). According to the study by Benavides et al., the active layer blend's reduced roughness can have a favorable effect on the charge transport pathways and carrier transport in OPDs.[59] The SA blend also has a finer interpenetrating network to promote efficient charge transport, according to a comparison of the phase images of the two different blends (Fig. S10(c-d)). Furthermore, the lower trap density could be a key factor in the improved

dynamic response of SA devices. Bogdan Vlad Popescu et. al found that the trap states have a profound influence on the -3dB frequency of organic photodiodes.[60, 61] As a result, in addition to morphological influence, the improved dynamic response of the 'SA' device could be attributed to the lower trap density.

We also calculated the resistance-capacitance (RC) time constant limited -3dB frequency of the 'SA' device using the following equation[62]

$$f_{RC} = \frac{1}{2\pi RC} \tag{6}$$

where R is the sum of the series resistance of the device (40 Ω) and load resistance of the oscilloscope (50 Ω), and C is the junction capacitance (0.45 nF) measured using inductance–capacitance–resistance (LCR) meter (Fig. S11). These values give rise to an RC constant of 41 ns and a corresponding f_{RC} value of 3.9 MHz. The aforementioned values suggest that the speed of the PD is not limited by the RC decay, but possibly by the transit time of the charge carriers.[62]

To have a good description of the thermal stability of an OPD, it is crucial to study the properties of the complete device. By employing s-EQE to track the defect states (before and after heating), it is feasible to study the increased heat stability of the 'SA' device in comparison to the 'control' device. Fig. S12 shows the s-EQE spectra in the range of 0.9-2 eV for both 'control' and 'SA' devices in a log scale. Upon 1 hour of heating at 100 °C, the s-EQE of the 'control' device shows an increase in the sub-gap region, while the low-energy tail of the ' SA' device does not have any major change after heating. This implies that the trap density in the 'control' device is increased after the heating process and this change is however not prominent in 'SA' devices These

results indicate that thermal stress-induced defect formation can be the primary reason for thermal degradation.

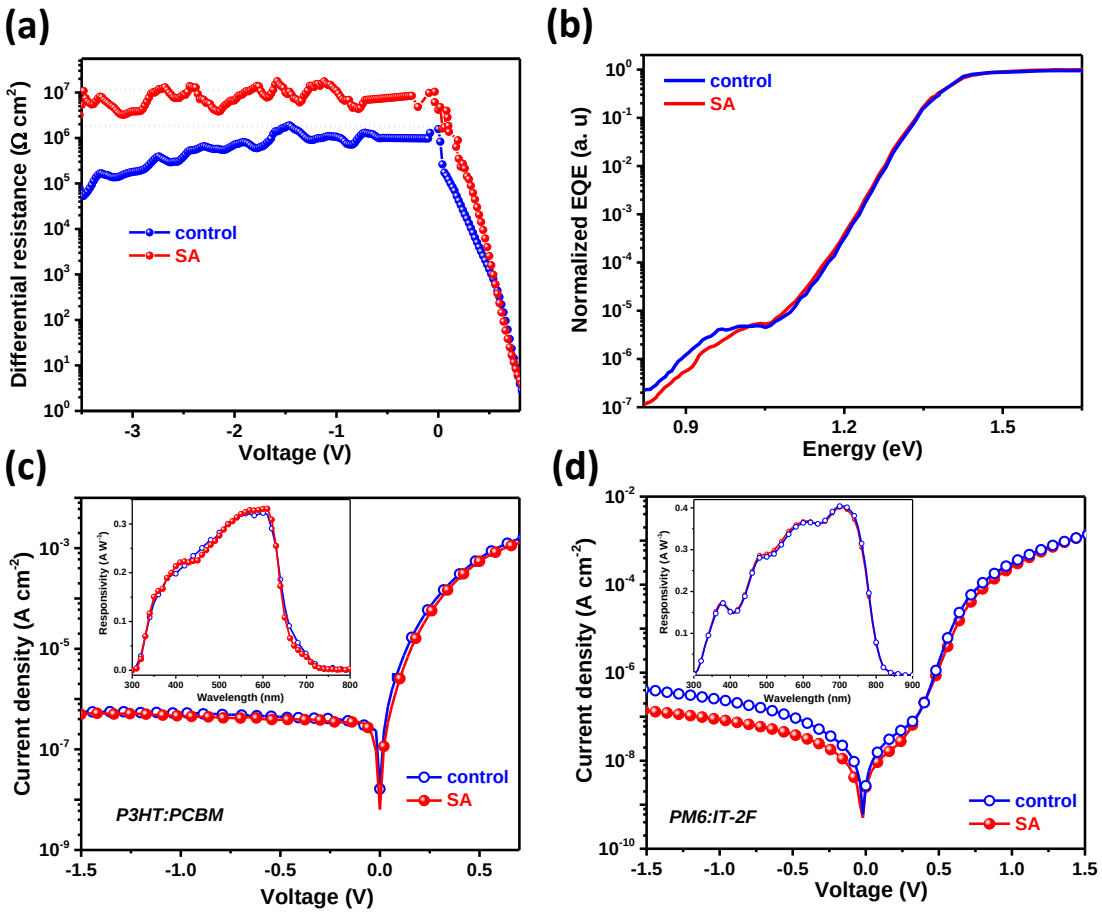

Fig. 4 (a) Differential resistance-voltage plot of 'control' and 'SA' devices (b) s-EQE spectra of the 'control' and 'SA' devices. Dark *J-V* curves of 'control' and 'SA' (c) P3HT:$PC_{71}BM$ and (d) PM6:IT-2F OPD devices. Inset is the responsivity of the corresponding devices.

Finally, the potential for the self-assembly processing technology to be applied in a variety of systems is also explored in a preliminary investigation. Representative systems were chosen from the classical fullerene (P3HT:$PC_{71}BM$) and non-fullerene (PM6:IT-2F) acceptor-based systems respectively. We kept the same device structure for 'control' and 'SA' devices as in the

case of the PM6:BTP-eC9 PD, except for the active layer employed. First, the widely investigated P3HT:$PC_{71}BM$ OPD system is fabricated in 'control' and 'SA' device architectures.[63] In terms of J_d and R (Fig. 4c), the 'SA' and 'control' devices are largely similar. Second, PM6:IT-2F system, a widely studied high-efficiency non-fullerene OPV system is considered for analysis. J_d of the 'SA' device (5.4 nA cm^{-2}) is lower than the two-step 'control' device (13 nA cm^{-2}) at -0.1V bias. R is indistinguishable for both types of devices (Fig. 4d). Preliminary studies (in terms of dark current and responsivity) on these systems show that the self-assembly OPD architecture performs on par with or better than the control device, and it may be applied to other OPD systems that use o-xylene, chlorobenzene, or 1,2-dichlorobenzene as the processing solvent.

Conclusion

We have demonstrated a simple self-assembly strategy that not only eases the fabrication of OPD, but also delivers robust stability and competitive performance. The presented proof-of-concept OPD device (PM6:BTP-eC9) showcases competitive performance metrics such as low noise current, responsivity approaching ~0.5 A/W and ultrafast temporal response comparable to commercial silicon diodes (rise time of 1.4 µs and -3dB frequency of ~300 kHz). While enabling a much easier fabrication, performance metrics of self-assembled devices are comparable to or better than the 'control' device, and more importantly, stability against operational stressors (both light and heat) has greatly enhanced. The improved performance of the 'self-assembly' device is mainly attributed to suppressed shunt pathways and lower trap density. Preliminary research in two additional exemplary systems hints the possibility for this approach to be used in other material systems to create cost-effective OPDs.

Author Contributions

H.T.C and H.T contributed equally to this work. G.L., H.T.C, and H.T. conceptualized the work and designed the experiments. H.T.C, and H.T. conducted device fabrication and data analysis. T.L., S.M., K.L., Z.L, J.H., Z.R., F.L., Y.C., P.W.K.F., S.W.T., and S.L contributed to materials characterization and data analysis. All authors discussed the results and commented on the paper. H.T.C wrote the main draft and G.L., H.T.C, and H.T. revised and finalized the manuscript.

Conflicts of interest

There are no conflicts to declare.

Acknowledgements

This work was supported by the following grants: Research Grants Council of Hong Kong (GRF grant 15221320, CRF C5037-18G), National Science Foundation of China (NSFC 51961165102), Shenzhen Science and Technology Innovation Commission (Project No. JCYJ 20200109105003940), The Sir Sze-yuen Chung Endowed Professorship Fund (8-8480) provided by the Hong Kong Polytechnic University and Postdoc Matching Fund scheme (1-W15V) from The Hong Kong Polytechnic University.

References

1. J. Kublitski, A. Hofacker, B. K. Boroujeni, J. Benduhn, V. C. Nikolis, C. Kaiser, D. Spoltore, H. Kleemann, A. Fischer and F. Ellinger, *Nat. Commun.*, 2021, **12**, 1-9.
2. P. C. Chow and T. Someya, *Adv. Mater.*, 2020, **32**, 1902045.
3. H. Guo, S. Saifi, K. Fukuda, H.-M. Cheng, Z. Lou and X. Xu, *Digit. Signal Process.*, 2021, 103145.
4. E. Saracco, B. Bouthinon, J. M. Verilhac, C. Celle, N. Chevalier, D. Mariolle, O. Dhez and J. P. Simonato, *Adv. Mater.*, 2013, **25**, 6534-6538.

5. A. Armin, M. Hambsch, I. K. Kim, P. L. Burn, P. Meredith and E. B. Namdas, *Laser Photonics Rev.*, 2014, **8**, 924-932.

6. L. Zhang, T. Yang, L. Shen, Y. Fang, L. Dang, N. Zhou, X. Guo, Z. Hong, Y. Yang and H. Wu, *Adv. Mater.*, 2015, **27**, 6496-6503.

7. A. Armin, R. D. Jansen-van Vuuren, N. Kopidakis, P. L. Burn and P. Meredith, *Nat. Commun.*, 2015, **6**, 1-8.

8. J. H. Kim, A. Liess, M. Stolte, A. M. Krause, V. Stepanenko, C. Zhong, D. Bialas, F. Spano and F. Würthner, *Adv. Mater.*, 2021, **33**, 2100582.

9. C. Fuentes Hernandez, W. F. Chou, T. M. Khan, L. Diniz, J. Lukens, F. A. Larrain, V. A. Rodriguez Toro and B. Kippelen, *Science*, 2020, **370**, 698-701.

10. H. Guo, S. Saifi, K. Fukuda, H. M. Cheng, Z. Lou and X. Xu, *Digit. Signal Process.*, 2021, 103145.

11. J. H. Kim, A. Liess, M. Stolte, A. M. Krause, V. Stepanenko, C. Zhong, D. Bialas, F. Spano and F. Würthner, *Adv. Mater.*, 2021, **33**, 2100582.

12. J. Huang, J. Lee, J. Vollbrecht, V. V. Brus, A. L. Dixon, D. X. Cao, Z. Zhu, Z. Du, H. Wang and K. Cho, *Adv. Mater.*, 2020, **32**, 1906027.

13. G. Liu, T. Li, X. Zhan, H. Wu and Y. Cao, *ACS Appl. Mater. Interfaces*, 2020, **12**, 17769-17775.

14. Z. Zhao, C. Xu, L. Niu, X. Zhang and F. Zhang, *Laser Photonics Rev.*, 2020, **14**, 2000262.

15. R. D. Jansen-van Vuuren, A. Armin, A. K. Pandey, P. L. Burn and P. Meredith, *Adv. Mater.*, 2016, **28**, 4766-4802.

16. C. Wang, X. Zhang and W. Hu, *Chem. Soc. Rev.*, 2020, **49**, 653-670.

17. S.-H. Lee, C. Lee, S. C. Yoon and Y.-Y. Noh, *Mater. Sci. Eng. R Rep.*, 2022, **147**, 100660.

18. P. Jacoutot, A. D. Scaccabarozzi, T. Zhang, Z. Qiao, F. Aniés, M. Neophytou, H. Bristow, R. Kumar, M. Moser and A. D. Nega, *Small*, 2022, **18**, 2200580.

19. W. Jang, S. Rasool, B. G. Kim, J. Kim, J. Yoon, S. Manzhos, H. K. Lee, I. Jeon and D. H. Wang, *Adv. Funct. Mater.*, 2020, **30**, 2001402.

20. J. Liu, M. Gao, J. Kim, Z. Zhou, D. S. Chung, H. Yin and L. Ye, *Mater. Today*, 2021.

21. C. Yan, S. Barlow, Z. Wang, H. Yan, A. K.-Y. Jen, S. R. Marder and X. Zhan, *Nat. Rev. Mater.*, 2018, **3**, 1-19.

22. P. Cheng, G. Li, X. Zhan and Y. Yang, *Nat. Photonics*, 2018, **12**, 131-142.

23. T. Klab, B. Luszczynska, J. Ulanski, Q. Wei, G. Chen and Y. Zou, *Org. Electron.*, 2020, **77**, 105527.

24. L. Hu, Y. Liu, L. Mao, S. Xiong, L. Sun, N. Zhao, F. Qin, Y. Jiang and Y. Zhou, *J. Mater. Chem. A*, 2018, **6**, 2273-2278.

25. H. T. Chandran, T. W. Ng, Y. Foo, H. W. Li, J. Qing, X. K. Liu, C. Y. Chan, F. L. Wong, J. A. Zapien and S. W. Tsang, *Adv. Mater.*, 2017, **29**, 1606909.

26. B. R. Sutherland, A. K. Johnston, A. H. Ip, J. Xu, V. Adinolfi, P. Kanjanaboos and E. H. Sargent, *ACS Photonics*, 2015, **2**, 1117-1123.

27. H. T. Chandran, T. Liu, D. Shen, Z. Guan, M. Li, J. Antonio Zapien, S. W. Tsang, M. F. Lo and C. S. Lee, *Solar RRL*, 2020, **4**, 2000245.

28. H. W. Li, Z. Guan, Y. Cheng, T. Lui, Q. Yang, C. S. Lee, S. Chen and S. W. Tsang, *Adv. Electron. Mater.*, 2016, **2**, 1600200.

29. Y. Zhang, K. Liu, J. Huang, X. Xia, J. Cao, G. Zhao, P. W. Fong, Y. Zhu, F. Yan and Y. Yang, *Nat. Commun.*, 2021, **12**, 1-13.

30. H. Tang, H. Chen, C. Yan, J. Huang, P. W. Fong, J. Lv, D. Hu, R. Singh, M. Kumar and Z. Xiao, *Adv. Energy Mater.*, 2020, **10**, 2001076.

31. H. Chen, D. Hu, Q. Yang, J. Gao, J. Fu, K. Yang, H. He, S. Chen, Z. Kan and T. Duan, *Joule*, 2019, **3**, 3034-3047.

32. D. Hu, Q. Yang, H. Chen, F. Wobben, V. M. Le Corre, R. Singh, T. Liu, R. Ma, H. Tang and L. J. A. Koster, *Energy Environ. Sci.*, 2020, **13**, 2134-2141.

33. L. Zhan, S. Li, X. Xia, Y. Li, X. Lu, L. Zuo, M. Shi and H. Chen, *Adv. Mater.*, 2021, **33**, 2007231.

34. Y. Cui, H. Yao, J. Zhang, K. Xian, T. Zhang, L. Hong, Y. Wang, Y. Xu, K. Ma and C. An, *Adv. Mater.*, 2020, **32**, 1908205.

35. A. Seitkhan, M. Neophytou, M. Kirkus, E. Abou-Hamad, M. N. Hedhili, E. Yengel, Y. Firdaus, H. Faber, Y. Lin and L. Tsetseris, *Adv. Funct. Mater.*, 2019, **29**, 1905810.

36. A. Kozbial, Z. Li, C. Conaway, R. McGinley, S. Dhingra, V. Vahdat, F. Zhou, B. D'Urso, H. Liu and L. Li, *Langmuir*, 2014, **30**, 8598-8606.

37. D. K. Owens and R. Wendt, *J. Appl. Polym. Sci.*, 1969, **13**, 1741-1747.

38. M.-C. Michalski, J. Hardy and B. J. Saramago, *J. Colloid Interface Sci.*, 1998, **208**, 319-328.

39. B. Janczuk and A. Zdziennicka, *J. Mater. Sci.*, 1994, **29**, 3559-3564.

40. C. N. Lam, R. Wu, D. Li, M. Hair and A. Neumann, *Adv. Colloid Interface Sci.*, 2002, **96**, 169-191.

41. W. Li, Y. Xu, X. Meng, Z. Xiao, R. Li, L. Jiang, L. Cui, M. Zheng, C. Liu and L. Ding, *Adv. Funct. Mater.*, 2019, **29**, 1808948.

42. A. Rogalski, *London—New York, CRC-Press Taylor Francis Group*, 2011.

43. Z. Zhong, F. Peng, Z. Huang, L. Ying, G. Yu, F. Huang and Y. Cao, *ACS Appl. Mater. Interfaces*, 2020, **12**, 45092-45100.

44. Y. Fang, A. Armin, P. Meredith and J. Huang, *Nat. Photonics*, 2019, **13**, 1-4.

45. C. Li, H. Wang, F. Wang, T. Li, M. Xu, H. Wang, Z. Wang, X. Zhan, W. Hu and L. Shen, *Light Sci. Appl.*, 2020, **9**, 1-8.

46. Z. Huang, Z. Zhong, F. Peng, L. Ying, G. Yu, F. Huang and Y. Cao, *ACS Appl. Mater. Interfaces*, 2020, **13**, 1027-1034.

47. Q. Burlingame, M. Ball and Y. L. Loo, *Nat. Energy.*, 2020, **5**, 947-949.

48. X. Xu, D. Li, J. Yuan, Y. Zhou and Y. Zou, *EnergyChem*, 2020, **3**, 100046.

49. J. Huang, J. Lee, H. Nakayama, M. Schrock, D. X. Cao, K. Cho, G. C. Bazan and T.-Q. Nguyen, *ACS nano*, 2021, **15**, 1753-1763.

50. Z. Lan, M.-H. Lee and F. Zhu, *Adv. Intell. Syst.*, 2021, 2100167.

51. C. G. Shuttle, N. D. Treat, J. D. Douglas, J. M. Fréchet and M. L. Chabinyc, *Adv. Energy Mater.*, 2012, **2**, 111-119.

52. C. Carati, L. Bonoldi and R. Po, *Phys. Rev. B*, 2011, **84**, 245205.

53. N. Zarrabi, O. J. Sandberg, S. Zeiske, W. Li, D. B. Riley, P. Meredith and A. Armin, *Nat. Commun.*, 2020, **11**, 1-10.

54. H. Thachoth Chandran, C. Yan and G. Li, *Adv. Energy Sustainability Res.*, 2022, 2200002.

55. A. Fallahpour, S. Kienitz and P. Lugli, *IEEE Trans. Electron Devices*, 2017, **64**, 2649-2654.

56. Y. Cheng, X. Liu, Z. Guan, M. Li, Z. Zeng, H. W. Li, S. W. Tsang, A. G. Aberle and F. Lin, *Adv. Mater.*, 2021, **33**, 2006170.

57. S. Khelifi, K. Decock, J. Lauwaert, H. Vrielinck, D. Spoltore, F. Piersimoni, J. Manca, A. Belghachi and M. Burgelman, *J. Appl. Phys.*, 2011, **110**, 094509.

58. K. Liu, Q. Liang, M. Qin, D. Shen, H. Yin, Z. Ren, Y. Zhang, H. Zhang, P. W. Fong, Z. Wu and G. Li, *Joule*, 2020, **4**, 2404-2425.

59. C. M. Benavides, S. Rechberger, E. Spiecker, M. Berlinghof, T. Unruh, M. Biele, O. Schmidt, C. J. Brabec and S. F. Tedde, *Org. Electron.*, 2018, **54**, 21-26.

60. B. V. Popescu, D. H. Popescu, P. Lugli, S. Locci, F. Arca, S. F. Tedde, M. Sramek and O. Hayden, *IEEE Trans. Electron Devices*, 2013, **60**, 1975-1981.

61. F. Arca, S. F. Tedde, M. Sramek, J. Rauh, P. Lugli and O. Hayden, *Sci. Rep.*, 2013, **3**, 1-5.

62. M. Biele, C. Montenegro Benavides, J. Hürdler, S. F. Tedde, C. J. Brabec and O. Schmidt, *Adv. Mater. Technol.*, 2019, **4**, 1800158.

63. G. Li, V. Shrotriya, J. Huang, Y. Yao, T. Moriarty, K. Emery and Y. Yang, *Nat. Mater.*, 2005, **4**, 864.